3D ROI Image Reconstruction from Truncated Computed Tomography

Anando Sen, *University of Houston,* Demetrio Labate, *University of Houston,* Bernhard G. Bodmann, *University of Houston,* Robert Azencott, *University of Houston and ENSC France*

Abstract

This paper introduces a novel method for accurate region-of-interest (ROI) reconstruction from 3D computed tomography (CT), consisting of a wavelet-based regularized iterative reconstruction procedure which is guaranteed to converge to an exact or highly accurate solution within the ROI. ROI tomography is motivated by the goal to reduce the overall radiation exposure when primarily the reconstruction of a specified region rather than the whole object is required. Our approach assumes that only the 3D truncated X-ray projections restricted to the ROI are known and does not assume any previous knowledge about the density function, except for standard assumptions about integrability and regularity needed to ensure that forward and backward transforms are well defined. The main original contributions of this paper are the novel regularized reconstruction algorithm for 3D ROI CT, the theoretical justification of its convergence and the detailed analysis of the stability of the reconstruction algorithm as a function of the size of the ROI. Another benefit of our approach is that it not limited to a specific mode of acquisition. The algorithm performance is validated on both phantoms and experimental data using various simulated acquisition geometries.

Index Terms

X-ray transform, Radon transform, 3D Computed Tomography, truncated tomography, region-of-interest tomography, wavelets

I. INTRODUCTION

Computed Tomography (CT) is a widely used medical imaging method which is employed to visualize interior organs within the human body and obtain information of their structural properties from a set of X-ray projections. Starting with its introduction in the 1970s, CT has become an essential tool in medical diagnostic and preventive medicine, and its use has increased very rapidly over the last two decades due

to technological advances which have made the procedure much more user-friendly to both patients and radiologists. In recent years, the application of CT has expanded even further due to the introduction of new imaging technology including 64-detector scanners for applications such as angiography [1], [2]. However, CT involves exposure of the patient to X-ray radiation, with associated health risks (in the form of radiation-induced carcinogenesis) essentially proportional to the levels of radiation exposure [3], [4]. Currently, an estimated 2% of cancers the United States may be attributed to the radiation from CT examinations [5].

In order to reduce the patient exposure to radiation in CT, different strategies have been explored such as using a small number of projections (e.g., a small set of orientations) or truncating the projections (e.g., projections restricted to a small region of interest). However, classical analytic image reconstruction formulas require complete projected data. If data are incomplete, the reconstruction problem becomes ill posed [6] and naive numerical reconstruction algorithms suffer from serious issues of instability and visual artifacts. In this paper, we will focus on the so-called *interior problem* or *ROI tomography*. This is a special case of the truncated-data problem, where only the projections through a specified ROI in the interior of the object to be examined are measured. Reconstruction methods for truncated-data problem can be generally divided into two classes: analytic reconstruction methods and algebraic (or iterative) reconstruction methods.

Analytic reconstruction methods have received particular attention during the last decade. Indeed, contrary to the traditional understanding that incomplete data reconstruction implies some type of approximation of the object to be reconstructed (cf. [7], [8]), in 2002 it was shown for the first time that, under specific conditions, one can analytically compute accurate partial reconstructions in dimension $n = 2$ from incomplete data [9]. Following this result, several methods have been introduced during the last decade aiming to derive highly accurate or exact ROI reconstruction formulas from partial data, mostly in 2D. Among the most notable contributions in this direction, we recall the fan-beam ROI reconstruction formula in [9] and its several variants and extensions (e.g., [10], [11]. For each specific mode of acquisition, these methods derive an analytic formula for partial reconstruction from incomplete measurements. Note that, typically, in addition to being dependent on a particular acquisition mode, these methods impose restrictions on the geometry of the ROI and require some prior knowledge of the object to be recovered. We refer to [8] for a more detailed review of analytic reconstruction methods from incomplete data.

Algebraic methods (also called iterative methods) provide an alternative approach for the reconstruction from truncated-data problem. They have the advantage that they can be applied to essentially any type

of acquisition mode, and prior knowledge can be easily incorporated into the algorithm if needed [12], [13]. The main limitation of these methods is that they are computationally intensive, especially for 3D data. On the other hand, advances in high-performance computing, such as GPU-based implementations, make algebraic methods increasingly more competitive [14], [15]. Furthermore, the combination of algebraic methods with the newly emerged ideas from compressed sensing has the potential to reduce the computational cost significantly [16], [17].

In this paper we introduce and analyze a novel method for the accurate ROI reconstruction from truncated 3D CT projections. Note that the 3D problem has particular relevance in several clinical applications. In particular, surgical implant procedures typically require a 3D image of the implant and, in these cases, 3D CT scans are highly preferable to 2D projections; in many case they are necessary to ensure the accurate positioning of the implant. Since 3D scans produce a considerable amount of radiation dose, the need to reduce radiation is particularly important in this setting.

The approach for 3D ROI tomography we will present is a streamlined and efficiently formalized version of the Iteration Reconstruction-Reprojection algorithm [18], [19], [20]. Our method consists essentially in the following steps: 1) X-ray CT projections P_0 are measured only for the X-ray passing through a given ROI; 2) the initial estimate of the image F_0 is obtained by back-projection from P_0 or through any reconstruction formula or algorithm known to be accurate for complete CT data, followed by a regularization; 3) F_0 is re-projected, that is, a new set of projections P_1 is computed by applying the forward transform to F_0. This procedure is repeated producing a sequence of estimated images F_k which converge to the 'true' solution F within the ROI. Note that this algorithm can be applied using any mode of acquisition for which an existing analytic reconstruction formula or program is known to accurately invert complete CT data. This is an important practical consideration since the proposed method can be used essentially as a *post-processing* stage combined with any current CT acquisition-reconstruction strategy which handles accurately complete CT data. In the following, the application of our method will be illustrated for three different modes of acquisitions, namely, spherical, spiral and circular acquisitions, combined with their respective reconstruction formulas.

Compared to the Iteration Reconstruction-Reprojection (IRR) algorithms previously published (dealing with the 2D case only), our approach includes a wavelet-based regularization step which is essential to ensure the *rapid* convergence of our algorithm. In fact, 'unregularized' IRR algorithms are unstable in general. We also present a theoretical analysis showing that the proposed method is guaranteed to converge inside the ROI, provided that the size of the ROI is sufficiently large. Furthermore we show how to determine the minimal radii of spherical ROI for which reconstruction remains accurate and
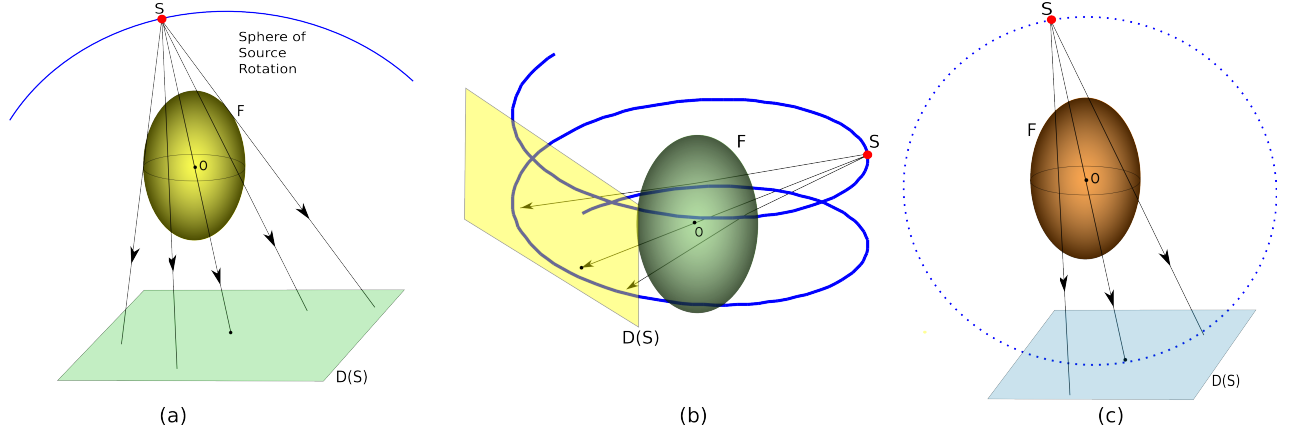
Fig. 1.   Data acquisition in different CT acquisition geometries, where radiations sources S are located: on (a) a spherical surface; (b) a spiral curve; (c) a circular curve.

feasible. We link these computations of critical ROI radii to the systematic analysis of the spectral radius for a specific linear operator. Note that the important problem of assessing the stability and accuracy of the reconstruction depending on the size of the ROI has received very little attention in the literature so far.

The rest of the paper is organized as follows. In Section II, we recall the definition of the X-ray transform and the related reconstruction formulas. In Section III, we describe the proposed algorithm for the ROI reconstruction from truncated 3D CT projections, including our regularization strategy. We also discuss the convergence properties of the algorithm. In Section IV, we illustrate the application of the proposed algorithm using different modes of acquisition and different geometries for the ROI. In particular, we examine the performance of the algorithm in terms of accuracy and theoretical exposure reduction, as well as its stability as a function of the size of the ROI. The Appendix contains the detailed mathematical analysis of the convergence properties of our reconstruction algorithm.

II. THE X-RAY TRANSFORM AND ITS INVERSE

X-ray tomography aims to reconstruct the unknown density function F of a 3D-object from a set of projection images of F obtained by measuring radiation attenuation along various straight line paths. If F is an integrable function, the *X-ray Transform* of F at (u, θ) is the line integral of F over the straight line (or *ray*) $l(u, \theta)$ through the point $u \in \mathbb{R}^3$ with direction $\theta \in S^2$, defined by

$$XF(u, \theta) = \int_{-\infty}^{\infty} F(u + t\theta) \, dt. \tag{1}$$

The problem of recovering F is formally solved by inverting the X-ray transform X and different inversion formulas have been derived depending on the particular acquisition geometry [21].

In the following, we assume that the support of the density function F is contained inside an open ball $B \in \mathbb{R}^3$ of radius ρ centered at the origin. For each θ in the unit sphere S^2, we denote by $T(\theta)$ the plane orthogonal to θ in $\mathbb{R}^3$. Hence, for $u \in T(\theta)$, we denote by (u, θ) the ray parallel to θ in $\mathbb{R}^3$ and passing through u. The set Ω of all rays passing through B has compact closure in $\mathbb{R}^4$ (because the set of u's is bounded) and thus Ω can be viewed as a 4-dimensional differentiable manifold, which can be identified with an open submanifold of the tangent space to S^2. This naturally defines a Riemannian volume element on Ω and the associated function spaces $L^p(\Omega)$, $1 \le p \le \infty$. For any $G \in L^p(\Omega)$, denote by G_θ the function defined on the plane $T(\theta)$ by $G_\theta(u) = G(u, \theta)$ and by $\|G_\theta\|_p$ the norm in $L^p(T(\theta))$ with the usual area measure.

We denote by $\mathcal{L}(B)$ the space of function in $L^2(B)$ such that the norm $\|f\|_{\mathcal{L}(B)} = \|f\|_{L^\infty(B)} + \|\Delta f\|_{L^\infty(B)} + \|\Delta^2 f\|_{L^\infty(B)}$ is finite. We adopt a similar notation for $\mathcal{L}(\Omega)$. The space $\mathcal{L}(B)$ is directly related to the Sobolev space $W^{4,\infty}(B)$: when all the partial derivatives of order up to 4 of a function f are in $L^\infty(B)$ then f is in $\mathcal{L}(B)$. The same statement is true for $\mathcal{L}(\Omega)$, when partial derivatives of f are computed in arbitrary smooth local coordinates on the manifold Ω. A direct computation shows that, for $F \in \mathcal{L}(B)$, the X-ray transform XF belongs to the space $\mathcal{L}(\Omega)$ and it satisfies

$$\|XF\|_{\mathcal{L}(\Omega)} \le c \, \|F\|_{\mathcal{L}(B)},$$

where the constant c depends only on ρ but not on F.

For any $G \in \mathcal{L}(\Omega)$, $\theta \in S^2$ and $v \in T(\theta)$, the 2-dimensional Fourier transform $\mathcal{F}_\theta$ of G_θ, is defined by

$$\mathcal{F}_\theta \, G_\theta(v) = \int_{T(\theta)} e^{-i\langle v, u \rangle} \, G_\theta(u) \, du.$$

A direct computation using the boundedness of B shows that

$$|\mathcal{F}_\theta \, G_\theta(v)| \le c \, (1 + |v|^4)^{-1} \|G\|_{\mathcal{L}(\Omega)} \quad \text{for all } v \in T(\theta), \tag{2}$$

for all $\theta \in S^2$, where the constant c depends only on ρ, but not on G.

Choose a fixed function $\theta(z) \in S^2$ such that $\langle z, \theta(z) \rangle = 0$ for almost all $z \in \mathbb{R}^3$. For all $G \in \mathcal{L}(\Omega)$, we define the function $X^{-1}G$ on $\mathbb{R}^3$ by

$$X^{-1}G(x) = (2\pi)^{-3} \int_{\mathbb{R}^3} e^{i\langle x, z \rangle} \, \mathcal{F}_{\theta(z)} \, G_{\theta(z)}(z) \, dz. \tag{3}$$

In view of (2), $X^{-1}G$ is bounded, continuous, and verifies

$$\|X^{-1}G\|_\infty \le c \, \|G\|_{\mathcal{L}(\Omega)}, \tag{4}$$

where the new constant c depends only on ρ but not on G. Note also that the Fourier transform $\mathcal{F}$ on $\mathbb{R}^3$ satisfies

$$\mathcal{F}X^{-1}G(z) = \mathcal{F}_{\theta(z)}\,G_{\theta(z)}(z), \quad \text{for all } z \in \mathbb{R}^3. \tag{5}$$

It is well known that, whenever $G = XF$ for some $F \in \mathcal{L}(B)$, formula (3) verifies the identity $X^{-1}G = F$. Hence, equation 3 explicitly reconstructs F from $G = XF$; that is X^{-1} is the (formal) *Inverse X-ray Transform*.

The inversion formula we have derived holds in the 'academic' setting where radiation sources are assumed to be positioned on a sphere completely surrounding the object. Note that the computation of this formula requires the knowledge of $G = XF$ for all directions $\theta \in S^2$ and locations $u \in T(\theta)$.

However, in any realistic data-collection setup, it is impractical or even impossible to compute XF for all values of (u, θ). Fortunately, there are rather simple conditions under which it is possible to recover F by placing the sources along a curve A around F. One of the first and most influential reconstruction formula for sources located on a curve is due to Tuy [22]. This result requires that a smooth source curve A, located outside the support of F, intersect each plane hitting supp F transversally. More precisely, let $a = a(t)$, $t \in I$, be a parametric representation of A and suppose that for all $x \in \text{supp } F$ and all $\theta \in S^2$ there exists a $t = t(x, \theta) \in I$ such that

$$a(t(x, \theta)) \cdot \theta = x \cdot \theta, \text{ and } a'(t(x, \theta)) \cdot \theta \neq 0.$$

Then F can be recovered as

$$F(x) = -i\,(2\pi)^{-\frac{3}{2}} \int_{S^2} \left(a'(t) \cdot \theta\right)^{-1} \frac{d}{dt}(\mathcal{F}(XF))(a(t), \theta)\, d\theta,$$

where $t = t(x, \theta)$. Since supp F is compact, this formula is valid, for example, when A is a spiral curve or a curve made of two circle contained in orthogonal planes.

Tuy's formula was historically one of the first "usable" inversion formulas appeared in the literature and many other exact reconstruction formulas can be related to or deduced from this approach, including Katsevich's formula for spiral tomography [23], [24], where radiation sources are located along a spiral curve.

As discussed in the Introduction, in this paper we will apply our new ROI reconstruction algorithm from truncated CT projections in combination with three different (simulated) acquisition geometries. Namely, we will consider sources located on (i) a sphere, (ii) a spiral curve and (iii) a circular curve. Figure 1 shows the physical setup for the three acquisition geometries.

A. Truncated X-ray Transform

Our goal is the reconstruction an unknown 3D density function F inside a specific ROI using truncated X-ray projections.

We assume that we only know the X-rays passing through a spherical *truncation region* C contained inside the support B of the density function F, as illustrated in Figure 2. The region C determines the set of all rays passing through C which are precisely the rays of the form (u, θ) with u in the planar disk $C(\theta)$, where $C(\theta)$ is the orthogonal projection of C on the plane $T(\theta)$. Accordingly, we define the *C-truncated X-ray transform Y* as the mapping from $F \in \mathcal{L}(B)$ into the function

$$YF(u, \theta) = 1_{C(\theta)}(u)XF(u, \theta). \tag{6}$$

It is useful to introduce a 'smoothed' version of the truncated X-ray transform. Given a spherical truncation region C and a spherical ROI $\tilde{C}$ strictly included in C, one can easily define for each $\theta \in S^2$ an explicit smooth function λ_θ approximating the indicator function of the circular corona $B(\theta) \setminus C(\theta)$. Namely, let $\lambda_\theta(u)$ be any C^∞ function of $(u, \theta) \in \Omega$, taking values in $[0, 1]$, such that $\lambda_\theta = 1$ on $B(\theta) \setminus C(\theta)$ and $\lambda_\theta = 0$ on $\tilde{C}(\theta)$. Then, for any function G on Ω and for a given $\theta \in S^2$, pointwise multiplication by λ_θ defines the linear operator $G \to \Lambda G$, by

$$[\Lambda G]_\theta = \lambda_\theta G_\theta. \tag{7}$$

It follows that $(I - \Lambda)$, where I is the identity operator, is a smoothed truncation operator associated to C and $\tilde{C} \subset C$. Hence we define the *smoothed C-truncated X-ray transform ZF* of F as the mapping on Ω given by

$$F \to ZF = (I - \Lambda)YF.$$

Note that ZF verifies the identity $ZF = XF - \Lambda XF$.

The following observation will be useful below. Call $s(\theta)$ the surface area of $B(\theta) \setminus C(\theta)$ in the plane $T(\theta)$. By construction, $\|\lambda_\theta\|_2$ is controlled by $\sqrt{s(\theta)}$ and we have:

$$\|[\Lambda G]_\theta\|_2 \leq \sqrt{s(\theta)} \, \|G_\theta\|_\infty. \tag{8}$$

III. ROI CT REGULARIZED RECONSTRUCTION

Our main objective is to obtain an accurate approximation of F *in the ROI $\tilde{C} \subset C$* from the truncated projections YF or their smoothed versions ZF. Due to the well known ill-posedness of the X-ray inversion formula, a direct reconstruction approach from truncated X-ray projections using a standard
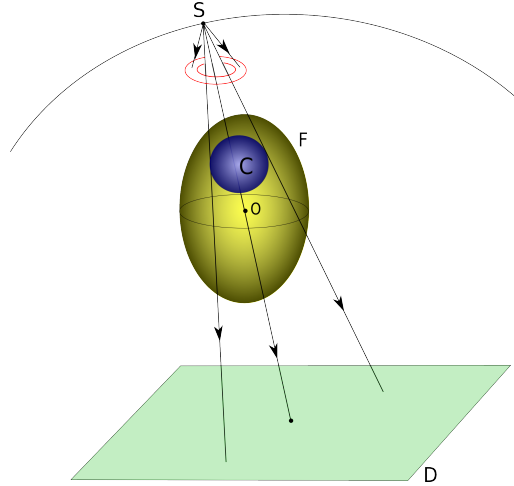
Fig. 2. Data acquisition using C-truncated 3D X-ray Tomography

inversion formula or algorithm for complete data is numerically unstable and produces highly inaccurate results.

As indicated above, our approach for ROI reconstruction is based on a refinement of the Iteration Reconstruction-Reprojection algorithm consisting of an iterative procedure where the reconstructed function F inside the ROI is successively updated while the function F outside the ROI is repeatedly regularized. One of the main novelties of our approach is the careful design of a regularization stage which is essential to ensure the convergence of the reconstruction algorithm and control the overall performance of the algorithm. Intuitively, the role of the regularization consists in ensuring that the solution of the inversion problem is well defined within a certain solution space. The rigorous analysis of the convergence properties is another main contribution of this paper.

A. A Regularized Reconstruction Algorithm of ROI CT Data

We adopt the notation introduced in Section II where X is the X-ray transform, X^{-1} its formal inverse and $Z = (I - \Lambda)$ the smoothed C-truncated X-ray transform. Also we denote by σ the *regularization operator*, where σ is the orthogonal projection of $L^2(\mathbb{R}^3)$ into a proper subspace. We will discuss below specific choices of σ.

Our *ROI CT algorithm* assumes that the projected data are known only inside the truncation region $C \subset B \subset \mathbb{R}^3$. Denoting by F the unknown density function having support inside B, the algorithm is initialized by computing

$$F_0 = \sigma X^{-1} Z F,$$

where ZF are the known data. In order to compute the next approximation of the solution we proceed as follows. We first re-project the image and split the projection into its smoothed C-truncated part and the complement as

$$XF_0 = (I - \Lambda)XF_0 + \Lambda XF_0 = ZF_0 + \Lambda XF_0.$$

Next we replace ZF_0 by the known data ZF and apply the inverse transform followed by the regularization operator σ, yielding

$$F_1 = \sigma X^{-1}ZF + \sigma X^{-1}\Lambda XF_0.$$

By repeating this procedure, we compute the iterative approximations F_n of the unknown F by

$$F_n = \sigma X^{-1}ZF + \sigma X^{-1}\Lambda XF_{n-1}. \tag{9}$$

It is important to notice that the operator X^{-1} appearing in the iterative procedure above can be interpreted as a *black box*, meaning that it could be any inversion formula for complete data or even a numerical inversion algorithm. In fact, as indicated in the introduction, we will apply the algorithm for several different acquisition geometries, using each time the corresponding forward and backward transform formulas.

B. Analysis of Convergence

We will show that the iterative reconstruction algorithm (9) converges to the exact solution or to an accurate approximation of the exact solution *inside the ROI* under fairly reasonable assumptions on the density functions F and the regularization operator σ. This is the content of the following theorem and corollary, whose proofs are found in the Appendix together with the discussion of some of its extensions.

Theorem 1. *Fix any finite dimensional vector space $V \subset \mathcal{L}(B)$ and let σ be the orthogonal projection of $L^2(\mathbb{R}^3)$ onto V. Let $C \subset B$ be a spherical truncation region and $(I - \Lambda)$ be the associated truncation operator, as in (7). Call $d(C, B) > 0$ the minimal distance between the points of C and the boundary of the ball B. Let X be the X-ray transform and X^{-1} be its classical inverse, given by (3). Then the linear operator $\mathcal{M} = \sigma X^{-1}\Lambda X$ maps V into V and there exists a constant $r > 0$ such that, whenever $d(C, B) < r$, then the operator $\mathcal{M}$ is a strict contraction in the L^∞–norm on V.*

Corollary 1. *Under the same assumptions as the theorem above, let $F \in \mathcal{L}(B)$ and assume that the C-truncated X-ray transform YF of F is known. Then the sequence F_n iteratively defined by the*

algorithm (9) *converges to a limit* F_∞ *in* $L^\infty(B)$, *at exponential speed. Moreover there is a finite constant* $\gamma = \gamma(r)$ *such that*

$$\|F_\infty - F\|_\infty \leq \gamma \|F - \sigma F\|_\infty$$

for all $F \in \mathcal{L}(B)$. *In particular, if* F *belongs to the regularization space* V, *then* F *must be identical to the algorithmic reconstruction* F_∞ *computed from the* C-*truncated X-ray transform* YF.

The truncation region C in Theorem 1 is chosen to be slightly larger than the ROI and must be strictly contained inside B. This is not a practical limitation as it simply requires that the set of X-ray source positions is taken to be disjoint from B.

Note that, in the statements above, the regularization operator σ is the orthogonal projection onto a finite dimensional subspace V of $L^2(B)$. When the density function F is in V, the algorithm is ensured to converge to F in L^∞ norm, and the sequence of approximate solutions F_n in (9) converges to the exact solution inside the ROI. When F is only assumed to be in $L^\infty(B)$, the algorithm is still guaranteed to converge, but the L^∞ distance between its limit and F is essentially of the same order as the L^∞ distance between F and its best approximation σF within V. As a consequence, the space V will typically be chosen to be a sufficiently 'large' subspace to ensure that it provides sufficiently good approximation of the density F to be reconstructed. These observations will be further illustrated in Section IV, where we show that our ROI reconstruction algorithm converges to an accurate approximation of the exact solution provided that the spherical region C containing the ROI is large enough.

Even though the statements above assume spherical CT acquisition, in Section IV we will apply our algorithm also to other acquisition geometries, such as the spiral and circular acquisitions. The current limitation of the theoretical result is due to the difficulty of the proof. It is possible to our theoretical results other acquisition geometries, such as the situation of sources located on a curve with the corresponding inversion formulas (e.g., Tuys formula). This requires a more careful mathematical analysis going beyond the scope of this paper and will appear elsewhere.

Theorem 1 implies an useful condition on the spectral radius of the operator $\mathcal{M}$. Recall that, for a bounded linear operator A, the *spectral radius* is the number

$$\rho(A) = \sup_{\ell \in s(A)} |\ell|,$$

where $s(A)$ is the spectrum of A. In the special case when A is an $n \times n$ matrix, then

$$\rho(A) = \max_i |\ell_i|,$$

where $\{\ell_i\}$ is the set of eigenvalues of A. The corollary below follows from the relationship between the contractivity of $\mathcal{M}$ and the spectral radius of $\mathcal{M}$.

Corollary 2. *Let $F \in \mathcal{L}(B)$ and $V \subset \mathcal{L}(B)$ be a finite dimensional subspace. Let X be the X-ray transform, X^{-1} be its inverse and σ be the orthogonal projection of $L^2(\mathbb{R}^3)$ onto V. For a spherical truncation zone $C \subset B$ and an ROI strictly contained in C, let $(I - \Lambda)$ be the associated truncation operator as in (7) and define $\mathcal{M} = \sigma X^{-1} \Lambda X$. Then the sequence of iterates (9) converges to σF within the ROI if and only if the spectral radius $\rho(\mathcal{M}) < 1$.*

Corollary 2 will be used in Section IV to numerically illustrate the convergence of our ROI reconstruction algorithm and discuss its properties as a function of the ROI radius.

C. Wavelet-based Regularization

As discussed above, the accuracy of our ROI reconstruction algorithm depends on the regularization operator σ which depends on the choice of the approximation space V.

Intuitively, the space V should be selected in such a way to provide good approximations for the class of density functions we intend to recover. In this paper, we consider a wavelet-based approach for the construction of the approximation space.

The main advantage of this approach is that wavelets provide *optimally efficient* approximations for a large class of functions, including functions in Besov and Sobolev spaces [25, Ch.9]. These spaces contain the type of functions which we have used to model the density functions of interest and for which the convergence properties discussed above have been shown to hold. Another useful property of wavelets is their ability to deal efficiently with discontinuities. This makes wavelet-based regularization methods generally preferable to SVD and other standard regularization methods which tend to smooth out reconstructed images with the consequence of causing a significant loss in accuracy especially near the edge points.

Let us briefly recall the main ideas about wavelet approximations (see [25] for more details). Given a generator $\Psi = \{\psi^1, \ldots, \psi^L\} \subset L^2(\mathbb{R}^n)$, a wavelet basis generated by Ψ is a collection of functions of the form

$$\{\psi_{j,k}^\ell(x) = 2^{\frac{nj}{2}} \psi^\ell(2^j x - k) : j \in \mathbb{Z}, k \in \mathbb{Z}^n, \ell = 1, \ldots, L\},$$

which forms an orthonormal basis of $L^2(\mathbb{R}^n)$. By choosing an appropriate well-localized generator Ψ, one can construct wavelet bases providing optimally sparse approximations for a large class of functions. That

is, it is possible to capture the main features of such functions by using only a small number of expansion coefficients. In practice, this is achieved by a simple procedure called *wavelet thresholding*, which consists in calculating the wavelet expansion of a function f and computing its compressed/regularized version as

$$\tilde{\sigma}f = \sum_{j \leq j_0} \sum_{k \in \mathbb{Z}} \sum_{\ell=1}^{L} c_{j,k,\ell}(f)\, \psi_{j,k}^{\ell}, \tag{10}$$

where $c_{j,k,\ell}(f) = \langle f, \psi_{j,k}^{\ell} \rangle$, if $|\langle f, \psi_{j,k}^{\ell} \rangle| \geq T_j$, and $c_{j,k,\ell}(f) = 0$ otherwise. In other words, the operator $\tilde{\sigma}$ projects f into a finite dimensional subspace V_f whose dimension is controlled by the *threshold* parameters T_j.

Note that the operator $\tilde{\sigma}$ in (10) is not linear and the corresponding subspace V_f depends on f. That is, if $f \neq g$ then the spaces V_f and V_g are different, in general. However, due to Theorem 1, after sufficiently many iterations, the approximate solutions F_n of the iterative algorithm (9) will stabilize. In other words, during the first set of iterations, the wavelet-based regularized reconstruction algorithm will 'search' for the correct approximation space. After, say, N iterations, the operator $\tilde{\sigma}$ will project all approximate solutions F_n, for $n > N$, into the same finite-dimensional approximation space V, according to Theorem 1.

In the next section, we present extensive numerical tests showing that the wavelet-based regularization approach performs very competitively in terms of accuracy and computational efficiency. In particular, this approach provides significantly more accurate reconstructions than simpler regularization schemes based on local averaging or low pass filtering. The superior performance is due to the higher flexibility provides by the wavelet approach for the selection of the approximation spaces.

IV. NUMERICAL RESULTS

In this section, we present several numerical experiments to illustrate the performance of the our ROI reconstruction algorithm from 3D truncated CT data.

For our experiments, we have used three sets of data, each one of size 256^3: a 3D Shepp-Logan phantom; a tissue from a mouse; a 3D scan of a human jaw. We simulated truncated data acquisitions using different acquisition geometries, namely, for source locations over a spherical surface, a spiral curve and a circular curve. We tested our algorithm for multiple spherical ROIs, centered at arbitrary locations inside the support of unknown density function F with ROI radii varying between 40 and 90 voxels. It was discovered experimentally (as discussed below) that the radius of 45 voxels is the minimal radius needed to ensure that our algorithm converges to accurate ROI reconstructions using data of the size we

(a) Phantom   (b) Mouse   (c) Jaw
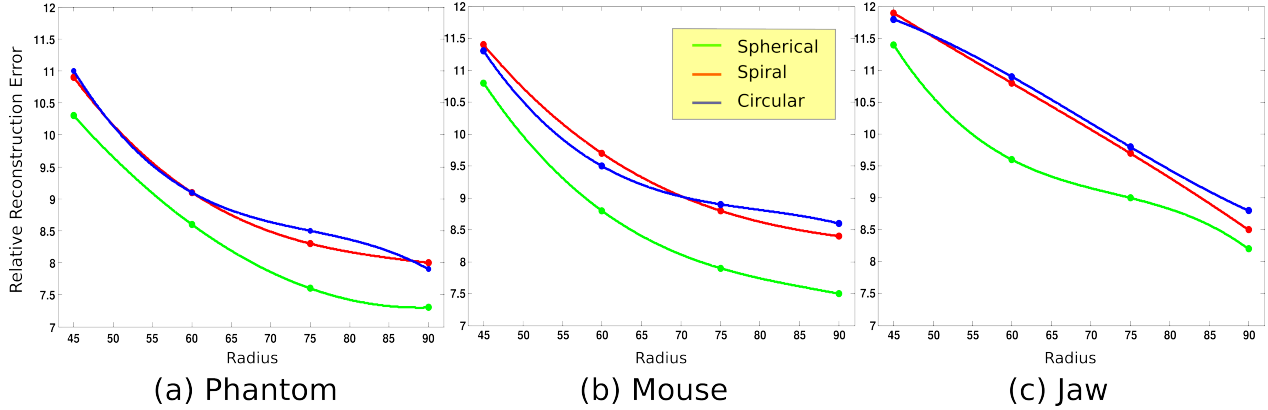
Fig. 3.   Curves of the Relative Reconstruction Errors for three data sets using different acquisition geometries. The data considered are: (a) Shepp-Logan phantom; (b) mouse tissue; (c) human jaw.

considered. For all our experiments, we stopped our algorithm after 40 iterations as this number was found to ensure the convergence of the algorithm (for ROI radius larger than 45 voxels).

For the regularization operator σ, we have used the wavelet-based approach described in Section III-C based on the thresholding operator (10), with the only difference that all coarse scale coefficients at scale $j \leq j_0$ were retained. The reason for keeping the coarse scale coefficients is that, in the reconstruction algorithm, σ acts locally" outside the region of interest. By keeping the coarse scale coefficients we are able to preserve all "global" features of the density function. For the wavelet decomposition, we have used standard Daubechies wavelets Daub4.

A. Numerical Analysis of Contractivity

We start by illustrating the convergence properties of our algorithm through the numerical analysis of the spectral radius ρ of the matrix $\mathcal{M} = \sigma X^{-1} \Lambda X$ associated with the algorithm (9).

To make this computation feasible, we will use matrices of small data size. Specifically, we will consider 3D discrete density functions supported in a cube B of 64^3 voxels. This implies that the density function can be viewed as a 3D image and hence as a vector in $\mathbb{R}^{262144}$. We consider the standard basis in this space, i.e., the set of matrices E_{ijk} whose entries are 1 at the (i, j, k)-th position and zeros everywhere else. We consider regions of interest with radii between 6 and 22 voxels and calculate the spectral radius for the operator $\mathcal{M} = \sigma X^{-1} \Lambda X$ where X and X^{-1} are the forward and backward transforms, respectively, for the various acquisition geometries considered.

The results in Table I show that the contractivity of the matrix $\mathcal{M}$ is ensured if the ROI radius is at

TABLE I

SPECTRAL RADIUS $\rho(M)$ OF M FOR VARIOUS ROI-RADII (OBJECT SIZE IS 64^3)

ROI-radius	6	10	13	14	18	22
Spherical Acquisition	10.62	9.33	4.15	0.90	0.74	0.66
Spiral Acquisition	15.27	8.54	4.07	0.94	0.83	0.73
Circular Acquisition	16.53	9.49	4.36	0.97	0.89	0.77

least 14 voxels. Note that this condition on the spectral radius is independent of the data and depends only on the data size, the ROI and the techniques of acquisition, inversion and regularization. By extrapolating from these results, we deduce that, for objects of size 256^3, the contractivity of $\mathcal{M}$ would be ensured provided the ROI radius is at least 56 voxels. This number is close to the value of 45 voxels which, as mentioned above, was found numerically in our experiments.

B. Algorithm Performance

To assess the accuracy of the reconstruction of our algorithm, we introduce the following notion of *Relative Reconstruction Error*. Specifically, let F be the density function to be recovered, where F is assume to be a bounded function with compact support in $\mathbb{R}^3$; let F_{rec} be an approximated reconstruction of F; and let C be a spherical region inside the support of F. The Relative Reconstruction Error Rel is defined as the number

$$Rel = \int_C \frac{|F(v) - F_{rec}(v)|}{|F(v)|} \, dv. \tag{11}$$

Figure 3 shows the plots for the Relative Reconstruction Errors for the there different density data as a function of the radius of the ROI. Each plot shows three curves, one for each of the three modes of acquisition. Note that the best performance of the algorithm occurs in the case of spherical acquisition, due to the fact that the larger number of projections makes the reconstruction from incomplete data more robust in this case. The performance of the algorithm is comparable in the cases of spiral and circular acquisitions. Also note that, for a fixed ROI radius, the Relative Reconstruction Error is lower in the case of phantom data and higher in the mouse and jaw data. This can be explained as follows.

As observed in the comments following the statement of Theorem 1, the ROI reconstruction algorithm converges to a regularized approximation σF rather than to the exact density function F in the ROI. As a consequence, the Relative Reconstruction Error can be broken up into two additive components, one due to the convergence error (we use only finitely many iterations) and another one due to the difference

between F and σF. To highlight the effect of the regularization, we computed the component of the relative reconstruction error due to the regularization, that is

$$Rel_\sigma = \int_C \frac{|F(v) - (\sigma F)(v)|}{|F(v)|}\, dv.$$

For the phantom, we found that $Rel_\sigma = 1.1\%$, while, for the mouse and jaw data sets, we found $Rel_\sigma = 2.4\%$. For example, in Figure 3, for ROI radius = 70, in the case of spherical acquisition, the Relative Reconstruction Error $Rel \approx 8\%$ for the Phantom data is approximately the sum of $Rel_\sigma = 1.1\%$ plus a term due to the convergence error $\approx 7\%$. In the case of Jaw data the two parts are approximately 2.4% and 6.6%. The lower value Rel_σ in the case of Phantom data is due to the fact that the piecewise constant data can be handled by the regularization operator much more effectively than more general data.

The quality of our ROI reconstruction algorithm from truncated projections is illustrated visual in Figures 6-11 for the Phantom and Mouse data. The figures show a baseline comparison of the ROI reconstructions obtained using our algorithm versus the standard unregularized reconstructions (using the formulas for the corresponding acquisition geometry considered). Each figure shows the horizontal middle slice extracted from the reconstructed 3D volumes in the cases of simulated acquisitions using spherical, spiral and circular acquisition modes. As expected, the standard unregularized ROI reconstructions from truncated projections are highly inaccurate and contain several visual artifacts. By contrast our algorithm is very accurate. For reference, the ground truth is also shown.

C. Exposure Reduction

Another measure of the performance of our algorithm is the lowering of radiation exposure due to the reduction of radiation sources. While a realistic estimation of the change in radiation exposure is beyond the scope of this paper, we consider here a very simplified model where the radiation dose $\delta(v)$ received by a voxel v is defined as the number of rays passing through v. Let $s = \sum_v \delta(v)$ be the sum of received doses over all pixels, in the case of collimated irradiation and m be the maximal dose which is received in the uncollimated case. We define the *Radiation Exposure RE*, as

$$RE = \frac{s}{m}. \tag{12}$$

Accordingly the *Exposure Reduction* is defined as $1 - RE$.

It is useful to examine the trade-off between Exposure Reduction and Reconstruction Error. As illustrated in Figure 4, it is possible to achieve a very significant reduction in the exposure at the expense
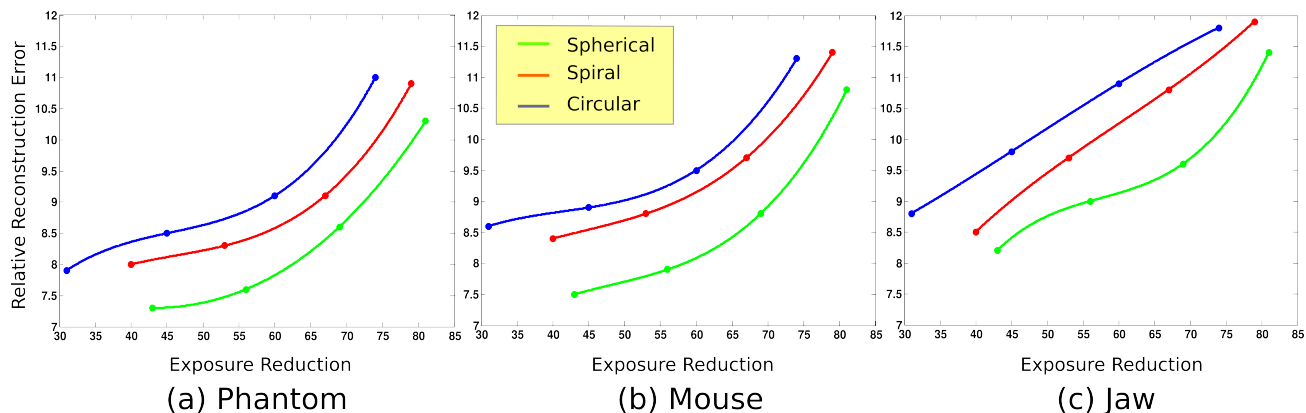
Fig. 4.   Relationship between Exposure Reduction and the Relative Reconstruction errors using different acquisition geometries for three data sets: (a) Shepp-Logan Phantom (b) Mouse Tissue (c) Human Jaw
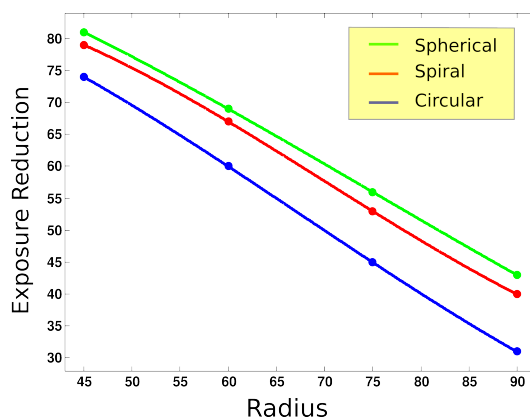

Fig. 5.   Exposure Reduction for various ROI radii using three acquisition geometries

of a limited loss of accuracy within the ROI. For example, in the case of Phantom data (see Figure 4 (a)), it is possible to have a value of about 60% of Exposure Reduction at the expense of only about 8% relative Reconstruction Error.

Figure 5 shows a plot of the Exposure Reduction as a function of the radius of the ROI in the three types of acquisition geometries. As expected, Exposure Reduction decreases as the radius of the ROI. Even though the exposure reduction depends in a complicated way on the acquisition geometry, the behavior of the curve is similar for the various acquisition geometries.

APPENDIX

In this section, we prove Theorem 1 and Corollary 1.

Fig. 6. Visual comparison of ROI reconstruction for the Shepp-Logan phantom using simulated spherical acquisition. A representative 2D slice is shown. From left to right: unregularized reconstruction; regularized ROI CT reconstruction; ground truth

Fig. 7. Visual comparison of ROI reconstruction for the Shepp-Logan phantom using simulated spiral acquisition. A representative 2D slice is shown. From left to right: unregularized reconstruction; regularized ROI CT reconstruction; ground truth

A. Proof of Theorem 1 and Corollary 1.

We start by making more explicit the inversion operator X^{-1} by specifying a measurable function $\theta(z) \in S^2$ for each $z \in \mathbb{R}^3$ such that $\langle z, \theta(z) \rangle \equiv 0$. For simplicity, we fix an arbitrary unit vector $\eta \in S^2$ and call $\mathcal{R}\eta$ the one-dimensional vector space generated by η. Let Γ be the 'equatorial circle' of all $\theta \in S^2$ such that $\langle \theta, \eta \rangle = 0$. Any vector $z \notin \mathcal{R}\eta$ then defines a unit vector $\theta(z) \in \Gamma$ by the normalized exterior product

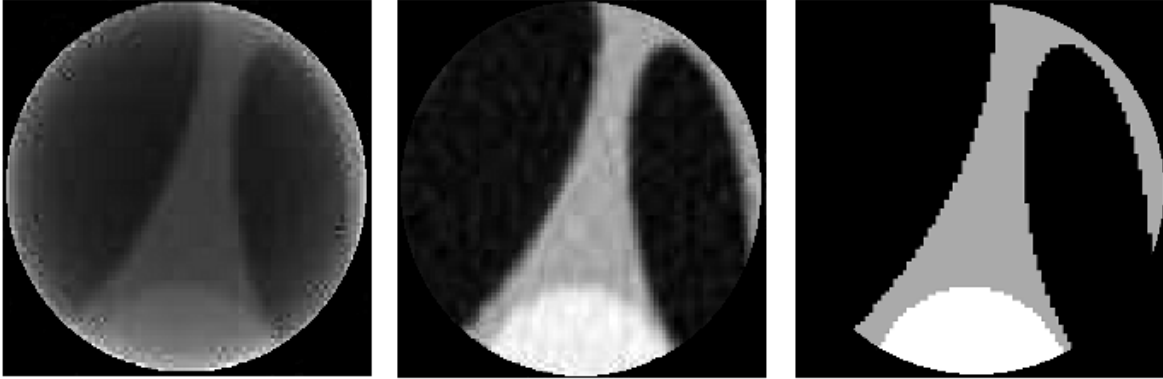$$\theta(z) = \frac{z \times \eta}{|z \times \eta|}.$$

Fig. 8. Visual comparison of ROI reconstruction for the Shepp-Logan phantom using simulated circular acquisition. A representative 2D slice is shown. From left to right: unregularized reconstruction; regularized ROI CT reconstruction; ground truth
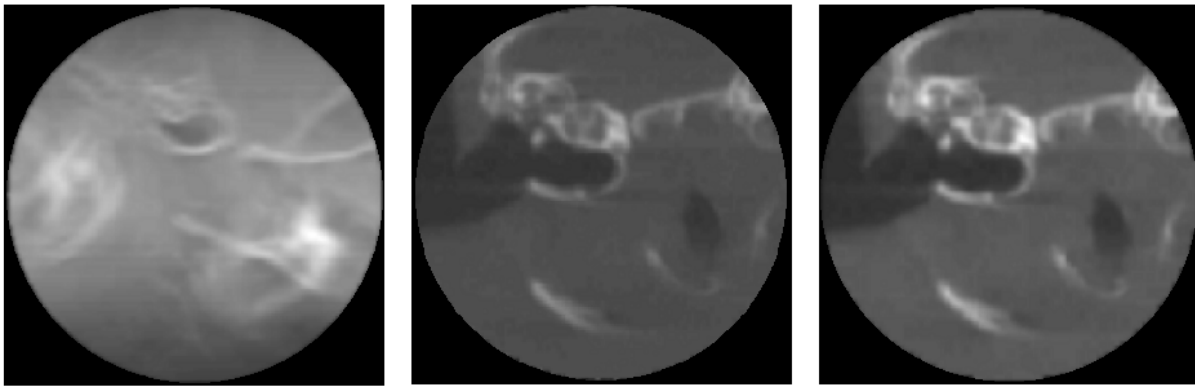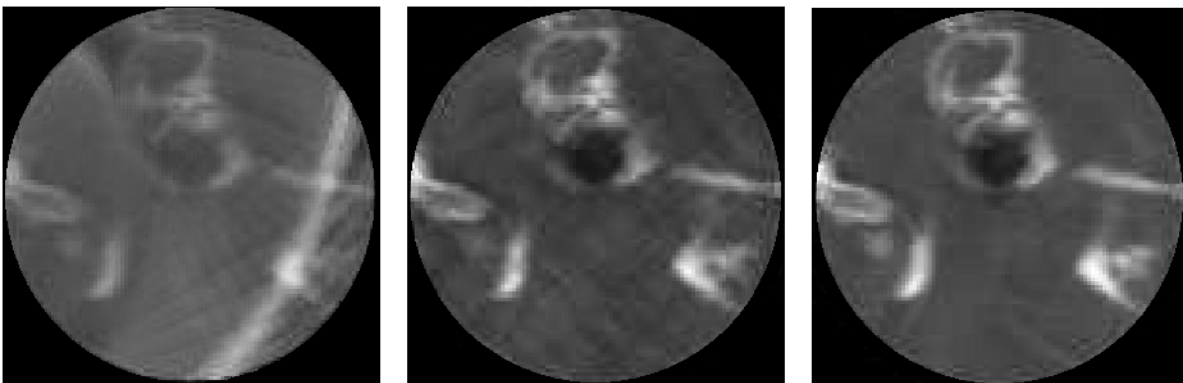

Fig. 9. Visual comparison of ROI reconstruction for the mouse tissue data using simulated spherical acquisition. A representative 2D slice is shown. From left to right: unregularized reconstruction; regularized ROI CT reconstruction; ground truth

Fig. 10. Visual comparison of ROI reconstruction for the mouse tissue data using simulated spiral acquisition. A representative 2D slice is shown. From left to right: unregularized reconstruction; regularized ROI CT reconstruction; ground truth
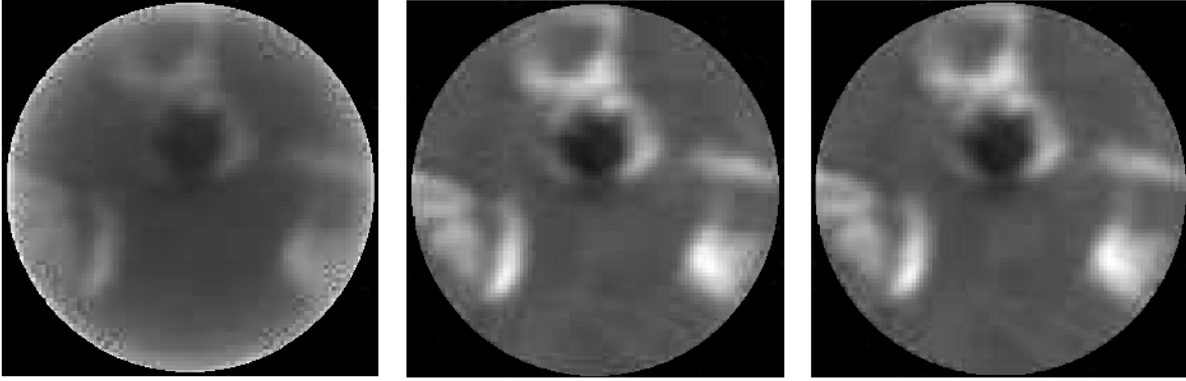
Fig. 11. Visual comparison of ROI reconstruction for the mouse tissue data using simulated circular acquisition. A representative 2D slice is shown. From left to right: unregularized reconstruction; regularized ROI CT reconstruction; ground truth

For $z \in \mathcal{R}\eta$, we set $\theta(z) = \zeta$ where ζ is an arbitrarily fixed unit vector orthogonal to θ. From now on, η, ζ, and the measurable function $\theta(z)$ just defined remain fixed, as well as the associated inversion operator X^{-1} given by (3). For $\varphi \in \mathcal{L}(B)$ and $G \in \mathcal{L}(\Omega)$, using equation (5), we have that:

$$
\begin{aligned}
\langle \varphi, X^{-1}G \rangle &= \langle \mathcal{F}\varphi, \mathcal{F}X^{-1}G \rangle \\
&= \int_{\mathbb{R}^3} \mathcal{F}\varphi(z)\, \mathcal{F}_{\theta(z)}\, G_{\theta(z)}(z)\, dz.
\end{aligned}
\tag{13}
$$

Note that here and below, the inner product is understood as inner product in $L^2(\mathbb{R}^3)$.

For any function $H \in L^1(\mathbb{R}^3)$, integration in cylindrical coordinates around the rotation axis η shows that

$$
\int_{\mathbb{R}^3} H(z)\, dz = \frac{1}{2} \int_\Gamma \int_{T(\theta)} H(v)\, |\langle v, \eta \times \theta \rangle|\, dv\, d\theta
\tag{14}
$$

so that equation (13) becomes

$$
\begin{aligned}
\langle \varphi, X^{-1}G \rangle &= \frac{1}{2} \int_\Gamma \int_{T(\theta)} |\langle v, \eta \times \theta \rangle|\, \mathcal{F}\varphi(v)\, \mathcal{F}_\theta G_\theta(v)\, dv d\theta \\
&= \frac{1}{2} \int_\Gamma \langle g_\theta, \mathcal{F}_\theta Z_\theta \rangle\, d\theta,
\end{aligned}
\tag{15}
$$

where, for each θ, the function $g_\theta \in L^2(T(\theta))$ is given by

$$
g_\theta(v) = |\langle v, \eta \times \theta \rangle|\, \mathcal{F}\varphi(v), \quad v \in T(\theta).
$$

In view of the bound for $|\mathcal{F}\varphi(v)|$ provided by equation (2), the function g_θ must verify

$$
\|g_\theta\|_2 \le c\, \|\varphi\|_{C^4} \quad \text{for all } \theta \in \Gamma,
$$

where the new constant c does not depend on φ.

From (15) it follows that, for all $G \in \mathcal{L}(\Omega)$ and all $\varphi \in \mathcal{L}(B)$,

$$
\begin{aligned}
|\langle \varphi, X^{-1}G \rangle| &\leq \frac{1}{2} \int_\Gamma \|g_\theta\|_2 \, \|\mathcal{F}_\theta G_\theta\|_2 \, d\theta \\
&\leq c \, \|\varphi\|_{C^4} \frac{1}{2} \int_\Gamma \|G_\theta\|_2 \, d\theta,
\end{aligned}
\tag{16}
$$

where the new constant c does not depend on φ or G.

Let $H \in V$. Using (8) and the elementary observation that, for each $\theta \in S^2$,

$$
\|X_\theta H\|_\infty \leq 2\rho \, \|H\|_\infty,
$$

it follows that the function $\Lambda X H$ satisfies

$$
\|[\Lambda X H]_\theta\|_2 \leq \sqrt{s(\theta)} \, \|X_\theta H\|_\infty \leq 2\,\rho\,\sqrt{s(\theta)} \, \|H\|_\infty,
\tag{17}
$$

where $s(\theta)$ is the surface area of the circular corona $B(\theta) \setminus C(\theta)$ in $T(\theta)$. Hence, for any $\varphi \in \mathcal{L}(B)$, using equations (16) and (17), we obtain:

$$
|\langle \varphi, X^{-1}\Lambda X H \rangle| \leq c\|\varphi\|_{C^4} \, \|H\|_\infty \int_\Gamma \sqrt{s(\theta)} \, d\theta.
\tag{18}
$$

For any function f on Γ, we have $\|f\|_1 \leq 2\pi \, \|f\|_2$. Hence

$$
\int_\Gamma \sqrt{s(\theta)} \, d\theta \leq \left(2\pi \int_\Gamma s(\theta) \, d\theta \right)^{1/2} = \sqrt{2\pi \, \mathrm{vol}(B \setminus C)},
$$

where $\mathrm{vol}(B \setminus C)$ is the volume of $(B \setminus C)$ in $\mathbb{R}^3$. Thus equation (18) now implies

$$
|\langle \varphi, X^{-1}\Lambda X H \rangle| \leq c \, \sqrt{\mathrm{vol}(B \setminus C)}\|\varphi\|_{C^4} \, \|H\|_\infty
\tag{19}
$$

where the new constant c depends on ρ but not on φ nor H.

The linear operator $\mathcal{M} = \sigma \, X^{-1} \Lambda \, X$ maps the finite dimensional regularization space V into itself. We are going to show that, if V is equipped with a suitable norm and the ROI radius satisfies certain assumptions, then $\mathcal{M}$ is a strict contraction.

Fix an orthonormal basis $\mathcal{B} = (\varphi_1, \dots, \varphi_N)$ of V. Select any function H in V, let $h = \mathcal{M}H$ and denote by $h_j = \langle \varphi_j, h \rangle$ the coordinates of h in the basis $\mathcal{B}$. Since σ is the orthogonal projection onto V, we must have $h_j = \langle \varphi_j, X^{-1}\Lambda X H \rangle$. Hence, due to equation (19), we have that for all $j = 1 \dots N$

$$
|h_j| \leq c \, \sqrt{\mathrm{vol}(B \setminus C)}\|\varphi\|_{C^4} \, \|H\|_\infty \leq c \, \sqrt{\mathrm{vol}(B \setminus C)} \, \kappa \, \|H\|_\infty,
\tag{20}
$$

where we have set $\kappa = \max_{j=1 \dots N} \|\varphi_j\|_{C^4}$.

For any $H \in V$, the expansion of $h = \mathcal{M}H$ in the basis $\mathcal{B}$ and (20) show that

$$
\begin{aligned}
\|\mathcal{M}H\|_\infty &= \|\sum_{j=1}^{N} h_j \varphi_j\|_\infty \\
&\leq \kappa \sum_{j=1}^{N} |h_j| \\
&\leq c N \kappa^2 \sqrt{\mathrm{vol}(B \setminus C)}\, \|H\|_\infty.
\end{aligned}
$$

Hence, once we endow the vector space $V \subset \mathcal{L}(B)$ with the norm of $L^\infty(B)$, we have that the operator norm of $\mathcal{M}$ is bounded by

$$
\|\mathcal{M}\| \leq c N \kappa^2 \sqrt{\mathrm{vol}(B \setminus C)}, \tag{21}
$$

where the constant c depends only on ρ. Thus, if $\sqrt{\mathrm{vol}(B \setminus C)}$ is smaller than $1/(cN\,\kappa^2)$, i.e., as soon as the truncation region C is large enough, the operator $\mathcal{M}$ will satisfy the contraction property $\|\mathcal{M}\| < 1$ on V.

In this situation, the ROI reconstruction algorithm (9) which generates a sequence of functions $F_n \in V$ verifying

$$
F_{n+1} - F_n = \mathcal{M}(F_n - F_{n-1})
$$

will converge at exponential speed in $L^\infty(B)$ to a limit $F_\infty \in L^\infty(B)$. Equation (9) then yields $(Id - \mathcal{M})F_\infty = \sigma X^{-1} Z F$. Since $ZF = XF - \Lambda XF$, this implies the relation $(I - \mathcal{M})F_\infty = \sigma F - \mathcal{M}F$ and entails the identity

$$
(I - \mathcal{M})(F_\infty - \sigma F) = \mathcal{M}(\sigma F - F).
$$

Since M is a contraction, $(Id - \mathcal{M})$ is invertible and

$$
\begin{aligned}
\|F_\infty - \sigma F\|_\infty &= \|(I - \mathcal{M})^{-1}\mathcal{M}(\sigma F - F)\|_\infty \\
&\leq \frac{\|\mathcal{M}\|}{1 - \|\mathcal{M}\|}\,\|\sigma F - F\|_\infty.
\end{aligned}
$$

This obviously yields

$$
\|F_\infty - F\|_\infty \leq \frac{1}{1 - \|\mathcal{M}\|}\,\|\sigma F - F\|_\infty,
$$

which concludes the proof.

To extend the theorem to density functions $F \in L^\infty(B)$ which are not smooth enough to be in $\mathcal{L}(B)$, we introduce on the space of rays Ω a family of smoothing kernels K_s, indexed by $s > 0$, which approximate the identity as $s \to 0$. Fix a nonnegative function $g \in C^\infty(\mathbb{R}^3)$, with compact support inside

the unit ball, verifying $g(0) = 1$ and $\int_{\mathbb{R}^3} g = 1$. For each $s > 0$ and each $H \in L^\infty(\Omega)$, we define the function $K_s H$ for $(u, \theta) \in \Omega$ by

$$K_s H(u, \theta) = \frac{1}{s^3} \int_{R^3} g(\tfrac{y}{s}) H(u - y + \langle y, \theta \rangle \theta, \theta) dy. \tag{22}$$

This is well defined because $v = (u - y + \langle y, \theta \rangle \theta)$ is orthogonal to θ, so that $(v, \theta) \in \Omega$. The linear operators K_s map $L^\infty(\Omega)$ into $\mathcal{L}(\Omega)$ and satisfy the "commutation" relation $K_s X = X G_s$, where X is the X-ray transform and the operator G_s is defined on $L^\infty(B)$ as the convolution with the function $\frac{1}{s^3} f(\frac{x}{s})$. Fix a small $s > 0$ and the smoothing kernel K_s as in (22). For each F in $L^\infty(B)$ with known C-truncated X-ray transform YF, we first smooth YF by K_s in order to compute F_0 by

$$F_0 = \sigma X^{-1} Z K_s Y F = \sigma X^{-1} (I - \Lambda) K_s Y F,$$

where we used the same notation as in Theorem 1. Then we can show the following.

Corollary 3. *Under the assumptions of Theorem 1, for $F \in L^\infty(B)$, the sequence of approximate solutions F_n generated by the algorithm (9), initialized with F_0, converges in $L^\infty(B)$ to a limit F_∞. Moreover, let $r = d(C, B)$ and ρ be the radius of B. There exists a constant $\eta = \eta(r, \rho)$ independent of F such that for each $F \in L^\infty(B)$ one can find $s(F) > 0$ for which the following L^2-norm inequality holds:*

$$\|F_\infty - F\|_2 \le \eta \|F - \sigma F\|_2, \quad \text{for all } s < s(F).$$

REFERENCES

[1] C. Herzog, P. L. Zwerner, and J. R. Doll et al., "Significant coronary artery stenosis: comparison on per-patient and per-vessel or per-segment basis at 64-section ct angiography," Radiology, vol. 244, no. 1, pp. 112–120, 2007.

[2] J. M. Miller, M. Dewey, and A. L. Vavere et al., "Coronary ct angiography using 64 detector rows: methods and design of the multi-centre trial core-64," Eur Radiol, vol. 19, no. 4, pp. 816–828, 2009.

[3] C. I. Lee, A. H. Haims, and E. P. Monico et al., "Diagnostic ct scans: assessment of patient, physician, and radiologist awareness of radiation dose and possible risks," Radiology, vol. 231, no. 2, pp. 393–398, 2004.

[4] W. Huda, W. Randazzo, and S. Tipnis et al., "Embryo dose estimates in body ct," AJR Am J Roentgenol, vol. 194, no. 4, pp. 874–880, 2010.

[5] D. Brenner and E. J. Hall, "Computed tomography. an increasing source of radiation exposure," N Engl J Med., vol. 357, pp. 2277–2284, 1997.

[6] F. Natterer, The Mathematics of Computerized Tomography. SIAM: Society for Industrial and Applied Mathematics, 2001.

[7] C. Berenstein and D. Walnut, "Local inversion of the radon transform in even dimensions using wavelets," in In 75 Years of Radon Transform, S. Gindikin and P. Michor, editors. International Press, 1992, pp. 45–69.

[8] R.Clackdoyle and M.Defrise, "Tomographic reconstruction in the 21st century. region-of-interest reconstruction from incomplete data," IEEE Signal Processing, vol. 60, pp. 60–80, 2010.

[9] F. Noo, M. Defrise, R. Clackdoyle, and H. Kudo, "Image reconstruction from fan-beam projections on less than a short scan," Physics in Medicine and Biology, vol. 47, no. 14, pp. 2525–2546, 2002.

[10] R.Clackdoyle and F. Noo, "A large class of inversion formulae for the 2-d radon transform of functions of compact support," Inverse Problems, vol. 20, pp. 1281–1291, 2004.

[11] Y. Zou, X. Pan, and E. Sidky, "Image reconstruction in regions-of-interest from truncated projections in a reduced fan-beam scan," Phys. Med. Biol., vol. 50, pp. 13–28, 2005.

[12] G. T. Herman and R. Davidi, "Image reconstruction from a small number of projections," Inverse Problems, vol. 24, no. 4, 2008.

[13] E. Sidky, C. Kao, and X. Pan, "Accurate image reconstruction from few views and limited angle data in divergent beam CT," Medical Physics, vol. 1, 2009.

[14] G. Yan, J. Tian, S. Zhu, C. Qin, Y. Dai, F. Yang, D. Dong, and P. Wu, "Fast Katsevich algorithm based on GPU for helical cone-beam computed tomography," Information Technology in Biomedicine, IEEE Transactions on, vol. 14, no. 4, pp. 1053–1061, 2010.

[15] D. Xiao, Y. Chen, B. Qian, L. Yang, and Y. Kang, "Cone-beam computed tomography reconstruction accelerated with cuda," in Biomedical Engineering and Informatics (BMEI), 2011 4th International Conference on, vol. 1, 2011, pp. 214–218.

[16] G. H. Chen, J. Tang, and S. Leng, "Prior image constrained compressed sensing (piccs): a method to accurately reconstruct dynamic CT images from highly undersampled projection data sets," Medical Physics, vol. 35, no. 2, pp. 660–663, 2008.

[17] H. Yu and G. Wang, "Compressed sensing based interior tomography," Physics in Medicine and Biology, vol. 54, pp. 2791–2805, 2009.

[18] M. Nassi, W. R. Brody, B. P. Medoff, and A. Macovski, "Iterative reconstruction-reprojection: An algorithm for limited data cardiac-computed tomography," Biomedical Engineering, IEEE Transactions on, vol. BME-29, no. 5, pp. 333–341, 1982.

[19] J. Kim, K. Y. Kwak, S.-B. Park, and Z. H. Cho, "Projection space iteration reconstruction-reprojection," Medical Imaging, IEEE Transactions on, vol. 4, no. 3, pp. 139–143, 1985.

[20] A. Ziegler, T. Nielsen, and M. Grass, "Iterative reconstruction of a region of interest for transmission tomography," Medical Physics, vol. 35, no. 4, pp. 1317–1327, 2008.

[21] F. Natterer and F. Wubbeling, Mathematical Methods in Image Reconstruction. SIAM: Society for Industrial and Applied Mathematics, 2001.

[22] H. Tuy, "An inversion formula for cone-beam reconstruction," SIAM Journal on Applied Mathematics, vol. 43, no. 3, pp. 546–552, 1983.

[23] A. Katsevich, "An improved exact filtered backprojection algorithm for spiral computed tomography," Advances in Applied Mathematics, vol. 32, pp. 681–697, 2004.

[24] S. Zhao, H. Yu, and G. Wang, "A unified framework for exact cone-beam reconstruction formulas." Medical physics, vol. 32, no. 6, pp. 1712–1721, Jun. 2005.

[25] S. Mallat, A Wavelet Tour of Signal Processing, Third Edition: The Sparse Way, 3rd ed.   Academic Press, 2008.